Materials Science & Engineering A 880 (2023) 145044

Contents lists available at ScienceDirect

Materials Science & Engineering A

journal homepage: www.elsevier.com/locate/msea

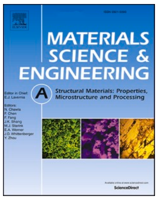

High deposition rate wire-arc directed energy deposition of 316L and 316LSi: Process exploration and modelling

Luc Hagen [a], Zhenzhen Yu [a], Amy Clarke [a], Kester Clarke [a], Stephen Tate [b], Anthony Petrella [a], Jonah Klemm-Toole [a,*]

[a] *Colorado School of Mines, Golden, CO, 80401, USA*
[b] *Electric Power Research Institute, Charlotte, NC, 28262, USA*

ARTICLE INFO

Keywords:
Wire arc additive manufacturing
Wire arc directed energy deposition
316L
316LSi
Microstructure modeling
Heat transfer modeling
Strengthening mechanisms

ABSTRACT

A parameter design of experiments was undertaken to study the impact of Si content in the wire feedstock, weld speed, and interpass temperature on the microstructure and mechanical properties of high deposition rate Wire-Arc Directed Energy Deposition (WA-DED) of 316L stainless steel. Small-scale, representative builds were constructed using a high deposition rate pulsed spray transfer mode. Across conditions, WA-DED 316L builds exceeded American Society of Mechanical Engineers (ASME) SA-240 minimum values for yield strength, elongation, and tensile strength at room temperature, tested both parallel and perpendicular to the build direction. It was found that 316LSi samples (higher Si content version of 316L) displayed significantly higher strengths and ductilities than samples produced with 316L, while the impact of weld speed and interpass temperature were less significant. A heat transfer model of the WA-DED process was created to allow for microstructure predictions. An infrared thermal camera system was used to calibrate this model by taking temperature measurements at fixed points during the deposition of several layers. Solidification models were developed to allow for predictions of microstructural features in the as-built condition. Predictions of dendrite spacings and growth morphologies show good agreement with experiments, demonstrating the potential for modeling the influences of the WA-DED parameters for process optimization. Based on microstructural analysis, it was concluded that the increase in strength and ductility in 316LSi compared to 316L is due to effects of composition on solid solution strengthening and stacking fault energy, suggesting opportunities for developing new stainless steel alloys for WA-DED with improved mechanical performance.

1. Introduction

Wire-arc directed energy deposition (WA-DED), or wire arc additive manufacturing (WAAM), is being considered as a fabrication method for pressure retaining components within nuclear power plants. This would allow for reduced lead time for fabrication of power plant replacement parts, decreased plant down time and potentially prevent millions of dollars in losses [1]. However, updates to the American Society of Mechanical Engineers (ASME) code are needed to use WA-DED to construct large 316L stainless steel pressure retaining components.

Austenitic stainless steels like 316L are ideal for power generation applications due to their combination of high corrosion resistance, strength/ductility balance, and good elevated temperature performance [2]. Additionally, 316L is a highly weldable alloy, making it an ideal candidate for WA-DED [3]. When compared to other metal additive manufacturing methods, WA-DED allows for rapid fabrication of larger parts, and the wire feedstock used is more economical than the powder used in other metal additive manufacturing processes. Parts produced with WA-DED show high density and good mechanical properties. However, due to the lower spatial resolution of WA-DED, finishing via machining is often required in addition to post-build heat treatment [4].

Understanding the solidification of 316L can provide valuable insights to the microstructure evolution of WA-DED 316L. Typically, the solidification of 316L follows a primary ferrite solidification pathway, where delta ferrite is the primary phase during solidification. During cooling, the delta ferrite experiences a solid-state transformation to austenite, which initially forms at the gap between ferrite dendrites. The solid-state transformation continues until ferrite only remains at the former dendrites cores in the form of skeletal (also called vermicular) delta-ferrite (δ) [3,5]. Delta ferrite in austenitic steels has been shown to

---

* Corresponding author.
E-mail address: jklemmto@mines.edu (J. Klemm-Toole).

https://doi.org/10.1016/j.msea.2023.145044
Received 16 February 2023; Received in revised form 11 April 2023; Accepted 12 April 2023

act as a strengthening phase [6].

After exposure to temperatures between 400 and 900 °C, delta ferrite can experience a transformation to the intermetallic sigma phase (σ). Sigma phase is a strong, brittle, chromium rich intermetallic phase, and its presence can negatively impact ductility and corrosion resistance. Due to the large heat input and slow cooling rates associated with WA-DED, it is expected that both delta ferrite and sigma phases will be observed in the as-built condition. Tuning the amount of these phases presents a method to improve the properties of WA-DED 316L after the build process. Chen et al. have previously studied how heat treatment of WA-DED 316L can be used to change amounts of ferrite and sigma phase present after the build process. Their results show that heat treatment can be used to effectively remove sigma phase from the 316L microstructure, with a corresponding drop in yield strength and ultimate tensile strength and an increase in ductility [7].

Microstructure and part performance of WA-DED 316L has also been shown to be affected by heat input resulting from deposition parameters. Heat input and interpass temperature has been previously shown to impact residual stresses and grain size, thus influencing mechanical properties [8–10]. Additionally, ferrite and sigma phase formation, along with dendrite spacing, is directly influenced by solidification conditions and subsequent cooling rates [3,6,11]. Understanding these process, structure, properties, and performance (PSPP) relationships will allow for the production of better performing WA-DED 316L parts. Additionally, much of the previous work with WA-DED of stainless steel focuses on deposition rates ranging from 1 to 3 kg/h [12,13], although higher deposition rates could allow for increased productivity and shorter build times.

In this study, we seek to better understand the PSPP relationship for WA-DED 316L through a systematic study of processing parameters and wire feedstock silicon content. The influence of various heat treatment temperatures is evaluated to select a post-build heat treatment regime for a parametric study exploring the influences of travel speed, interpass temperature, and wire selection between 316L and 316LSi on microstructure and tensile properties. Additionally, a heat transfer finite element (FE) model was developed to understand the thermal history experienced by WA-DED builds. Analytical solidification models in combination with transfer simulations were used to predict the microstructure in the WA-DED builds from the parametric study.

2. Experimental methods

2.1. Build parameters and wire compositions

To construct builds, a Lincoln Electric S500 Power Wave gas metal arc welding (GMAW) power source with a RapidX pulsed spray transfer mode was used. For the wire feedstock, Lincoln Electric Blue Max® MIG 316L with a 1.14 mm (0.045 in) diameter was used with a feed rate of 1.02 m/min (400 in/min), resulting in a deposition rate of approximately 5 kg/h. A 95% Ar + 5% CO_2 shielding gas with a flow rate of 11.8 liters/min (25 feet^3/hour) was used during deposition. Builds were also constructed with 316LSi filler metal, using Lincoln Electric Red Max® MIG 316LSi with a 1.14 mm (0.045 in) diameter. The compositions of both wire feedstocks are shown in Table 1. Compositions of builds are shown in the Results section. To study the impact of heat treatment on WA-DED 316L, single bead wide builds measuring 12.7 cm × 10.2 cm x 0.9 cm (5 in x 4 in x 0.35 in) were constructed using 316L filler metal.

2.2. Processing parameter experimental design

A full factorial design was undertaken to study the impacts of travel speed, interpass temperature, and wire Si content. Builds were constructed with a size of 22.9 cm wide x 11.5 cm tall x 1.14 cm thick (9 in x 4.5 in x 0.45 in) on a 316L base plate. To produce builds wide enough to accommodate the extraction of tensile specimens, the GMAW torch path was weaved, as outlined in Table 2. Weave parameters changed with build parameter to keep the bead width at a constant value of 1.14 cm (0.45 in) across build conditions. Build parameters for the full factorial design of experiments are presented in Table 3.

The high and low levels for each build parameter were dictated by the useable window for build construction. At travel speeds lower than 50.8 cm/min (20 in/min), molten metal in the builds would sag on the sides of the build. At speeds higher 63.5 cm/min (25 in/min), the track welding system could not weave at the necessary velocity to maintain a 1.14 cm (0.45 in) build width. The 350 °C temperature was based on the highest interpass temperature that could be consistently controlled with the system used for these builds, while the 100 °C interpass temperature was set as the lowest temperature at which the cooling time was reasonable for build construction. Interpass temperatures were monitored using an optical pyrometer pointing at the middle width of the build.

2.3. Post-build heat treatment

To study post build heat treatment response, samples from build condition 1 from Table 3 were removed from the base plate and heat treated at 900, 1040, and 1200 °C for 1 h in air using a Carbolite CWF 13/5 furnace and water quenched. This range of heat treatment temperatures was selected based on results reported by others on WA-DED 316L [7,16,17]. The 1040 °C temperature was chosen based on the minimum heat treatment temperature specified by the American Society for Testing and Materials (ASTM) wrought 316L material [18]. The results from these experiments were used to down select a heat treatment regime for the parametric study.

2.4. Tensile testing

For the post-build heat treatment study, subsized, round tensile bars were machined from each of the heat-treated builds, oriented parallel to

Table 2
Weave parameters for DOE builds.

Material	Travel Speed	Weave Velocity	Weave Amplitude
316L	50.8 cm/min (20 in/min)	134.6 cm/min (53 in/min)	0.69 cm (0.27 in)
316L	63.5 cm/min (25 in/min)	198.2 cm/min (78 in/min)	0.76 cm (0.30 in)
316LSi	50.8 cm/min (20 in/min)	114.3 cm/min (45 in/min)	0.53 cm (0.21 in)
316LSi	63.5 cm/min (25 in/min)	165.1 cm/min (65 in/min)	0.71 cm (0.28 in)

Table 1
Typical wire composition (wt %) of Lincoln Electric Blue Max® MIG 316L [14] and Lincoln Electric Red Max® MIG 316LSi reported by the wire feedstock manufacturer [15].

	%C	%Cr	%Cu	%Mn	%Mo	%N	%Nb	%Ni	%P	%S	%Si
Lincoln Electric Blue Max® MIG 316L	0.01–0.02	18.5–18.7	0.03–0.13	1.6–1.8	2.1–2.6	0.03	0.01 max.	11.8–12.2	0.02	0.01 max	0.39–0.40
Lincoln Electric Red Max® MIG 316LSi	0.01–0.02	18.2–18.3	0.07–0.10	1.7	2.3	0.06–0.07	0.01 max.	11.3	0.02	0.02	0.79–0.87

Table 3
Build conditions for parameter study.

Build	Wire	Travel Speed	Interpass Temperature
1	316L	50.8 cm/min (20 in/min)	350 °C
2	316L	63.5 cm/min (25 in/min)	350 °C
3	316L	50.8 cm/min (20 in/min)	100 °C
4	316L	63.5 cm/min (25 in/min)	100 °C
5	316LSi	50.8 cm/min (20 in/min)	350 °C
6	316LSi	63.5 cm/min (25 in/min)	350 °C
7	316LSi	50.8 cm/min (20 in/min)	100 °C
8	316LSi	63.5 cm/min (25 in/min)	100 °C

the build direction, and tensile tested in accordance with ASTM E8 [19]. Following construction of the processing conditions shown in Table 3, each build was sectioned, with a portion kept in the as-built condition and another portion heat treated at 1040 °C for 1 h and water quenched. Tensile specimens were then machined out of the builds as shown in Fig. 1(a). From each build, 10 flat tensile bars were cut out, 5 in the build direction and 5 in the transverse direction, with 1 tensile bar in each direction from the as-built condition and 4 tensile bars from the heat-treated condition. The flat subsized tensile specimens were machined in accordance with ASTM E8 as shown in Fig. 1b.

Tensile testing was performed at a strain rate of 1×10^{-3} s^{-1} on an MTS Landmark 22.5 kip load frame using a 25.4 mm (1 in) gauge length extensometer in accordance with ASTM E8 [19]. For the post-build heat treatment study, two replicate tensile tests were performed for each condition at room temperature. For the builds generated in the parametric study in the heat-treated condition, two replicate tensile tests were performed from each sample orientation at room temperature. In the as-built condition, one tensile test was performed in each sample orientation at room temperature. An additional two replicate samples in the heat-treated condition from each sample orientation were tensile tested at 427 °C (800 °F), which is the maximum temperature required for time-independent properties within the American Society for Mechanical Engineers (ASME) code. Samples tested at elevated temperatures were heated using a thermocouple-controlled induction heater. Thermocouples were welded to samples prior to testing.

2.5. *Microstructure characterization*

Metallographic specimens were sectioned from each condition and polished to a final step of 0.05 μm diamond or colloidal silica. Electron backscatter diffraction (EBSD) using a JEOL 7000F field-emission scanning electron microscope (SEM) operating at 20 kV with a 15 mm working distance was performed to analyze the microstructure of the builds. Grain structure was examined by etching polished specimens with a Beraha 1 reagent, made up of 100 ml deionized water, 20 ml HCL, 2.4 g NH_4FHF, and 0.6 g $K_2S_2O_5$, to reveal grain boundaries [20]. A glyceregia etchant, composed of 15 ml HCL, 10 ml Glycerol, and 5 ml of HNO_3, was used to reveal dendritic structures [21]. Etched micrographs were taken using an Olympus DSX500 optical microscope. Grain size measurements were made from images collected from samples etched with the Beraha 1 reagent. Due to the columnar nature of the grains observed, grain width was calculated for grain size measurements. Grain width was calculated by overlaying horizontal lines across each micrograph and totaling the number of grain boundaries intersected by these lines using ImageJ software. The line distance was then divided by the number of grain boundaries to give an average grain width. Approximately 50 grains were measured to estimate grain size for each condition. Dendrite arm spacing was measured from images etched with the glyceregia etchant. At least 10 measurements of primary and secondary dendrite arm spacing were taken from each condition.

2.6. *Heat transfer model of WAAM process*

The weaved WA-DED builds were modeled in the commercial finite element software, Abaqus (v.2021). The 3D heat conduction equation was solved using a transient heat transfer simulation and mass transfer was modeled using the built-in element activation features of Abaqus/Standard. Convection within the molten pool was neglected. The latent heat of fusion was not modeled explicitly, but the heat required for phase transformation was considered by defining specific heat as a function of temperature through the solidus-liquidus transition [22,23]. Thermal conductivity [23,24] and density [22] were also temperature dependent.

Convection and radiation boundary conditions were prescribed on the top and side surfaces of the substrate and evolving free surfaces of the build volume. The bottom surface of the substrate was treated as insulated. The reference (i.e., far-field ambient) temperature for the purpose of convection and radiation boundary conditions was defined as 26 °C. The convection coefficient was $36{*}10^3$ (mW/mm^2 °C). The emissivity ratio for radiation heat transfer was 0.28 [24].

Heat input was modeled by a moving source with a double ellipsoid power density distribution defined by Goldak and Akhlaghi [25].

$$q_{(f/r)} = \frac{6\sqrt{3}f_{(f/r)}Q}{a_{(f/r)}bc\pi\sqrt{\pi}} exp\left[\frac{-3x^2}{a^2_{(f/r)}}\right] exp\left[\frac{-3y^2}{b^2}\right] exp\left[\frac{-3z^2}{c^2}\right] \tag{1}$$

$$f_f + f_r = 2 \tag{2}$$

Where q is power density (mW/mm^3) and mutually exclusive subscripts f and r refer to front or rear halves of the double ellipsoid, respectively. The dimension a (mm) was measured along the length of the power density distribution, which was aligned with the local x-axis and parallel to the path of the moving heat source. Dimensions b and c (mm) defined the width and depth of the power density field, respectively. Parameter f

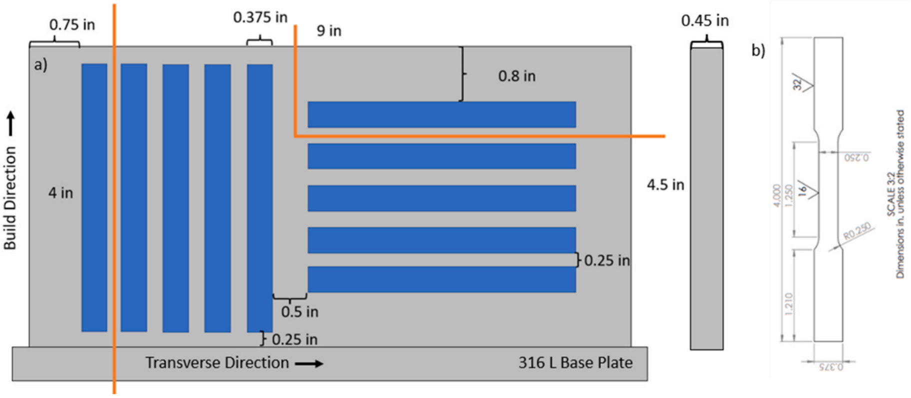

Fig. 1. (a) Schematic of builds used for the parametric study showing tensile bar layout and sectioning. Sectioning lines are marked in orange and indicate the portions of the build that were kept in the as built condition. b) Drawing of the ASTM E8 specimen machined from the builds. Dimensions are in inches.

was the power fraction, the values of which in the front and rear regions of the power distribution must obey Equation (2) [25]. Values of f_f and f_r in the present study were defined by the following relations,

$$f_f = 2\left(\frac{a_f}{a_f + a_r}\right) \tag{3}$$

$$f_r = 2\left(\frac{a_r}{a_f + a_r}\right) \tag{4}$$

Total power input Q (mW) was defined by,

$$Q = \eta \times V \times I \tag{5}$$

where η is arc efficiency, V (V) is voltage, and I (A) is current for the WA-DED process. Parameters a, b, and c, were estimated from visual inspection of the experimental conditions and all heat source parameters are summarized in Table 4.

For simplicity, the arc path was modeled as a straight line in the heat transfer simulation. The parameters of the heat source were adjusted to result in melt pool dimensions similar to the weaved heat source in the experiment. Nodal temperature data were extracted from the melt pool region on the top layer of the WA-DED deposition, and these data were used for later computation of temperature gradient, solidification velocity, and cooling rate. Time histories of nodal temperature were also extracted for fixed points on the lateral surface of the simulated build volume for validation comparison with experimental measurements. The setup of the model is illustrated in Fig. 2.

A Xiris XIR-1800 short wavelength infrared thermal camera was used to measure temperatures during WA-DED to calibrate heat transfer simulations. Video capture was performed at 1000 frames per second from a sideview with a focal distance of 400 mm. Video was captured to record four deposition passes with a 30 s interpass time. Emissivity was set to 0.9 based on work done by Valiorgue et al. [26]. Additional thermal images were taken to capture the top of the build to record melt pool shape.

2.7. Microstructure development models

The Kurz, Giovanola, Trivedi (KGT) dendrite growth model was used to predict the solidification structure in the WA-DED builds [27]. The model's simplified form, assuming constant solute diffusivities, partitioning coefficients, and liquidus slopes, can be solved analytically using Equations (6)–(12).

$$4\pi^2\Gamma\left(\frac{1}{R^2}\right) + \left(2\sum\left[m_i Pe_i(1-k_i)C_i^*\xi_i\right]\right)\left(\frac{1}{R}\right) + G = 0 \tag{6}$$

$$\xi_i = 1 - \frac{2k_i}{\sqrt{1+\left(\frac{2\pi}{Pe_i}\right)^2} - 1 + 2k_i} \tag{7}$$

$$Pe_i = \frac{RV}{2D_i} \tag{8}$$

$$C_i^* = \frac{C_o}{1 - [(1-k_i)Iv(Pe_i)]} \tag{9}$$

$$\Delta T_{c,i} = m_i\left(C_o - C_i^*\right) \tag{10}$$

$$\Delta T_r = \frac{2\Gamma}{R} \tag{11}$$

$$\Delta T_{total} = \sum_i \Delta T_{c,i} + \Delta T_r \tag{12}$$

In Equations (6)–(12), Γ is the Gibbs-Thomson coefficient; R is the dendrite tip radius; m_i is the liquidus slope for a given solute; k_i is the partition coefficient for a given solute; D_i is the interdiffusion coefficient of a given solute in the liquid; Pe_i is the Peclet number for a given solute; C_i^* is the composition of a given solute in the liquid at the dendrite tip; V is solidification velocity; C_o is the bulk composition of a given solute, G is the temperature gradient within the liquid, ΔT_r is curvature undercooling, $\Delta T_{c,i}$ is constitutional undercooling from a given solute; ΔT_{total} total liquid undercooling; ξ is a stability parameter; and Iv is the Ivanstov function. To solve these equations, a few key material values are needed. Gibbs-Thomson coefficient and liquid diffusivity values were found in literature [28,29] while partition coefficient and liquidus slope values were determined using ThermoCalc© 2021a using the TCFE11 database based on measured compositions of the builds (Table 9 in the Results section). The KGT model was implemented to reflect the contributions of six primary solutes within the alloy: Cr, Ni, Mo, Mn, Si, C.

To predict primary dendrite arm spacing (PDAS), the model proposed by Kurz was used, where the primary arms are assumed to be paraboloids in a hexagonal array. The dendrite tip is modeled to follow kinematics as described by a simplified LGK model [27,30,31,32]. Equation (13) gives the resulting relationship between the dendrite tip radius (R), dendrite tip temperature (T_{tip}), dendrite base temperature (T_{base}), temperature gradient (G), and PDAS (λ_1). To accommodate multicomponent alloys and a dendrite tip temperature that varies with solidification velocity, Equation (14) is used. A power law fit of dendrite tip radius as a function of solidification velocity is taken from the KGT model, and α_1 and β_1 are the coefficient and exponent from that fit, respectively. Similarly, a power law fit of total undercooling as a function of velocity is taken from the KGT model, and α_2 and β_2 are the coefficient and exponent, respectively. The non-equilibrium freezing range, $\Delta T_o'$ is determined from a Scheil simulation using ThermoCalc©.

$$\lambda_1 = \sqrt{\frac{3R\left(T_{tip} - T_{base}\right)}{G}} \tag{13}$$

$$\lambda_1 = \sqrt{\frac{3\left(\alpha_1 V^{\beta_1}\right)\left(\Delta T_o' - \alpha_2 V^{\beta_2}\right)}{G}} \tag{14}$$

Secondary dendrite arm spacing (SDAS) evolves throughout solidification due to coarsening. An SDAS model for multicomponent systems from Easton et al. [33] was used, as shown in Equation (15). The terms in Equation (15) have the same meanings as in Equations (6)–(14), and $c_{f,i}$ is the composition of a given solute in the liquid at the end of solidification. Scheil simulations in ThermoCalc© were used to obtain $c_{f,i}$ for each solute.

$$\lambda_2 = 5.5\left(\frac{M\Delta T_o'}{GV}\right)^{\frac{1}{3}} M = \frac{-\Gamma}{\sum\frac{m_i(1-k_i)\left(c_{f,i}-c_{o,i}\right)}{D_i}} \ln\left[\frac{\sum\frac{m_i(1-k_i)c_{f,i}}{D_i}}{\sum\frac{m_i(1-k_i)c_{o,i}}{D_i}}\right] \tag{15}$$

A columnar to equiaxed transition (CET) model was also used following the Gäumann modification to the original Hunt model, as shown in Equation (16) [34,35]. This modification assumes that all nucleation sites activate once the liquid undercooling reaches a critical undercooling for nucleation, ΔT_{nuc}. With this, temperature gradient, G, can be calculated as a function of total undercooling, ΔT_{total}, as shown in

Table 4
Heat source parameters for the WA-DED simulation performed in Abaqus.

Parameter	a_f (mm)	a_r (mm)	b (mm)	c (mm)	f_f	f_r	η	V (V)	I (A)
Value	5.3	10.6	4.6	2.34	0.67	1.33	0.85	22	210

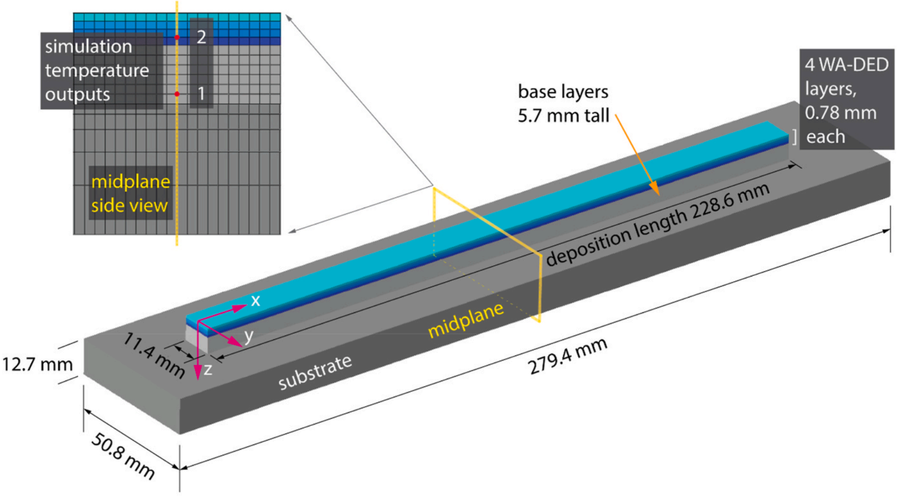

Fig. 2. Set up for heat transfer model, showing travel path as well as location from which nodal temperature information was extracted from. Locations 1 and 2 are from the bottom and top of the first deposition pass, respectively.

Equation (16). Nucleation site density, N_0, was estimated based on experimental measurements of grain size using the relationship in Equation (18).

$$G=\frac{1}{n+1}\sqrt[3]{\frac{-4\pi N_o}{3\,ln[1-\varnothing]}}\Delta T_{total}\left(1-\frac{\Delta T_{nuc}^{n+1}}{\Delta T_{total}^{n+1}}\right) \quad (16)$$

$$\Delta T_{total}=(aV)^{\frac{1}{n}} \quad (17)$$

$$N_0\sim\frac{1}{\sqrt[3]{grain\ size}} \quad (18)$$

In Equations (16) and (17), $\varnothing$ is the volume fraction of equiaxed grains, and a and n are material dependent constants which are found from a power law fit of total undercooling as a function of solidification velocity from the KGT model shown in Equation (17).

3. Results

3.1. Selection of post build heat treatment

Fig. 3 illustrates the EBSD inverse pole figure (IPF) and phase maps from heat-treated builds. Each condition displays large, columnar grains typically associated with WA-DED [7,36,10] with no obvious changes in grain structure across the conditions explored. However, the amount of sigma and delta phases present varies with heat treatment temperature. In the as built condition, austenite grains show skeletal ferrite dendrite cores with sigma also present at the dendrite cores, similar to reported by Chen et al. [7]. Upon heat treatment at 900 °C, much of the delta ferrite transforms to sigma phase at the dendrite cores. Others have reported significant increases in sigma content after heat treatment of WA-DED 316L between 800 and 1000 °C [7,16,17]. After heat treatment at 1040 °C, very little sigma is present, while similar amounts of delta ferrite are present compared to the as-built condition. Rodriquez et al. also reported no sigma phase after annealing WA-DED 316L at 1050 °C for 1 h [17]. Lastly, the sample heat treated at 1200 °C shows an almost completely austenitic microstructure, similar to results reported by others [7,16,17]. Table 5 summarizes the phase fractions for each condition.

The yield strength (YS), ultimate tensile strength (UTS), total elongation, and reduction in area for the heat-treated builds are given in

Table 5
Phase amount in volume % of the as built condition and after heat treatment for 1 h and water quenching at 900 °C, 1040 °C and 1200 °C.

Condition	Austenite	Ferrite	Sigma
As Built	95.7	3.6	0.7
900 °C	95.1	0.1	4.8
1040 °C	96.3	3.6	0.1
1200 °C	99.9	0	0.1

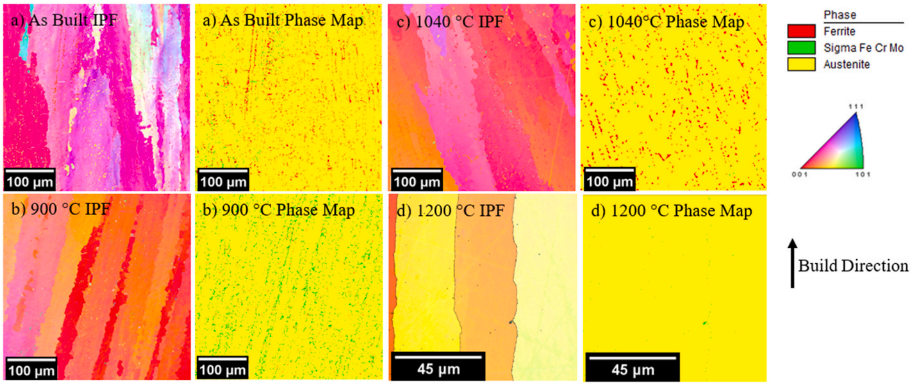

Fig. 3. EBSD IPF and phase maps of a) the as built condition and after heat treatment for 1 h and water quenching at b) 900 °C c) 1040 °C d) and 1200 °C. The IPF map is oriented to the build direction.

Table 6. Of the heat-treated conditions, 900 °C showed the highest tensile strength but also the lowest ductility. This is attributed to the increased amount of sigma phase in this condition. At 1040 °C, there is a reduction in tensile strength and an increase in ductility when compared to the 900 °C condition. This is likely due to the near elimination of brittle sigma phase. There is not a statistically significant difference in yield strength between the 900 °C and 1040 °C heat treated conditions. The as-built condition and the 1040 °C condition show similar amounts of ferrite, but the 1040 °C displayed higher ductility, likely due in part to the reduced amount of sigma phase. The increase in ductility from the as-built condition to the 1040 °C condition may also be a result of a reduction in dislocation density. Heat treatment in ranges of 1000 °C–1100 °C has been shown to relieve residual stresses and increase ductility in laser melted 316L [37], and others have reported decreases in dislocation density in the same temperature range [16]. The 1200 °C conditions showed a near fully austenitic structure, corresponding to the highest ductility of all the heat treatments evaluated. This condition also displayed the lowest YS and UTS of all conditions. The low strength is attributed to a greater reduction of dislocation density as well as the lack of ferrite to act as a strengthening phase in this condition [6].

From these results, the 1040 °C heat treatment was selected due to the best combination of strength and ductility to be used for the parametric study. The 1040 °C heat treat provided a significant increase in ductility over the as built and 900 °C conditions while maintaining relatively high yield and tensile strengths.

3.2. Parameter design of experiments – mechanical properties

Fig. 4 shows tensile strength, yield strength, and total elongation for conditions tested at room temperature in the parametric study along with minimum values according to ASME SA-240 [38] for 316L. The heat-treated specimens successfully meet ASME minimums for 316L across conditions, while the as built specimens fail to meet elongation requirements as outlined by SA-240 after adjustment for the 24.4 mm (1 in) gauge length using ISO 2566 [39]. The increase in ductility after heat treatment is in line with the results from heat treatment builds and indicates that heat treatment is a vital step for WA-DED 316L to meet mechanical property requirements.

In the as-built condition, very few of the parameters evaluated showed statistically significant influences on strength when tested at room temperature as indicated in Fig. 4. The 316LSi composition shows a higher ultimate tensile strength compared to 316L. Samples built with a lower interpass temperature showed higher yield strengths than those built at the higher interpass temperature. All of the other parameters did not have a statistically significant influence on strength and ductility in the as-built condition when tested at room temperature. In the heat-treated condition, the 316LSi composition shows a statistically significant increase in YS, UTS, and ductility over 316L, as shown in Fig. 4. However, travel speed and interpass temperature did not demonstrate a statistically significant effect on mechanical properties. It appears that the influence of interpass temperature on the YS in the as built condition is eliminated after post build heat treatment.

Fig. 5 summarizes the tensile properties of samples tested at 427 °C (800 °F) in comparison to ASME Section II typical values [40]. Samples successfully exceeded typical values for YS but did not meet UTS typical values. At 427 °C, the only significant effect is that 316LSi samples show higher UTS values than 316L samples. No other factors were shown to have a statistically significant impact on YS, UTS, or elongation in the heat treated condition when tested at 427 °C (800 °F).

Table 6
Mean tensile strength, yield strength, total elongation and reduction in area with 95% confidence limits calculated from pooled standard deviations from two replicates of each heat treated condition.

	Ultimate tensile Strength (MPa)	Yield Strength (MPa)	Total Elongation (%)	Reduction in area (%)
As Built	522 ± 30	304 ± 8	33 ± 13	52 ± 11
900 °C	589 ± 30	273 ± 8	34 ± 13	55 ± 11
1040 °C	505 ± 30	273 ± 8	42 ± 13	78 ± 11
1200 °C	484 ± 30	245 ± 8	51 ± 13	75 ± 11

3.3. Parameter design of experiments – microstructure characterization

To better understand the increase in strength associated with the 316LSi wire composition, a grain size comparison between heat treated 316L and 316LSi was undertaken. Due to the columnar nature of the grains, grain width was measured from etched micrographs of representative samples (Fig. 6), and Table 7 summarizes these results. There is not a statistically significant difference between the grain size of 316L and 316LSi in the as-built condition. Furthermore, the grain size is not significantly altered by the post-built heat treatment. It can therefore be assumed that there is a negligible difference in grain size between all the conditions evaluated in this study.

To assess the influence of solidification conditions on the microstructure, dendrite spacing measurements were made from each condition (Fig. 7), and these results are summarized in Table 8. No statistically significant differences in primary or secondary dendrite arms spacings were measured between the conditions evaluated.

Additionally, composition analysis was performed on both 316L and 316LSi WA-DED samples using both an optical emission spectrometer and LECO Combustion units (for oxygen, nitrogen, and carbon), and the results are shown in Table 9. This compositional information is used for solidification model development.

3.4. Temperature measurements of the WA-DED build process

A thermal camera video was recorded to capture temperatures during deposition of four consecutive layers for heat transfer model calibration. All temperature information was captured using 316L wire and corresponding weave parameters from Table 3. Because a constant dwell time between passes is needed for the heat transfer model, experiments were conducted with the appropriate dwell time to achieve either 100 or 350 °C interpass temperatures. Video was recorded for a 63.5 cm/min travel speed, 30 s interpass time; a 50.8 cm/min, 30 s interpass time; and a 63.5 cm/min, 3 min interpass time. A 30 s interpass time corresponds to the 350 °C interpass temperature, while a 3 min time corresponds with a 100 °C interpass temperature. Two point temperature measurements were taken during the build process as shown in Fig. 8a, the results were compared to equivalent positions in the heat transfer model shown in Fig. 8b.

4. Discussion

4.1. Heat transfer model calibration

The heat transfer model was calibrated with temperature data captured from thermal camera video. Fig. 9 shows recorded temperature measurements from points shown in Fig. 8, in comparison with predicted temperature from the thermal model for four deposition passes. In the initial passes the model predicts a cooling rate slower than that measured, as can be seen by comparing the slopes of the temperature vs time curves. Subsequent passes show better agreement between the model and experiment, particularly for measurement point 2. The discrepancy between the modeled and measured temperatures is likely due to how the weave was modeled. To simplify the model, a wider, non-weaving heat source was used, keeping the center of the heat source in the center of the melt pool. In the experiment, a weaving heat source was used, leading to the center of the heat source nearing the edge of the wall. This likely results in the higher experimental measurement observed, as well as contributing to differences between model melt pool

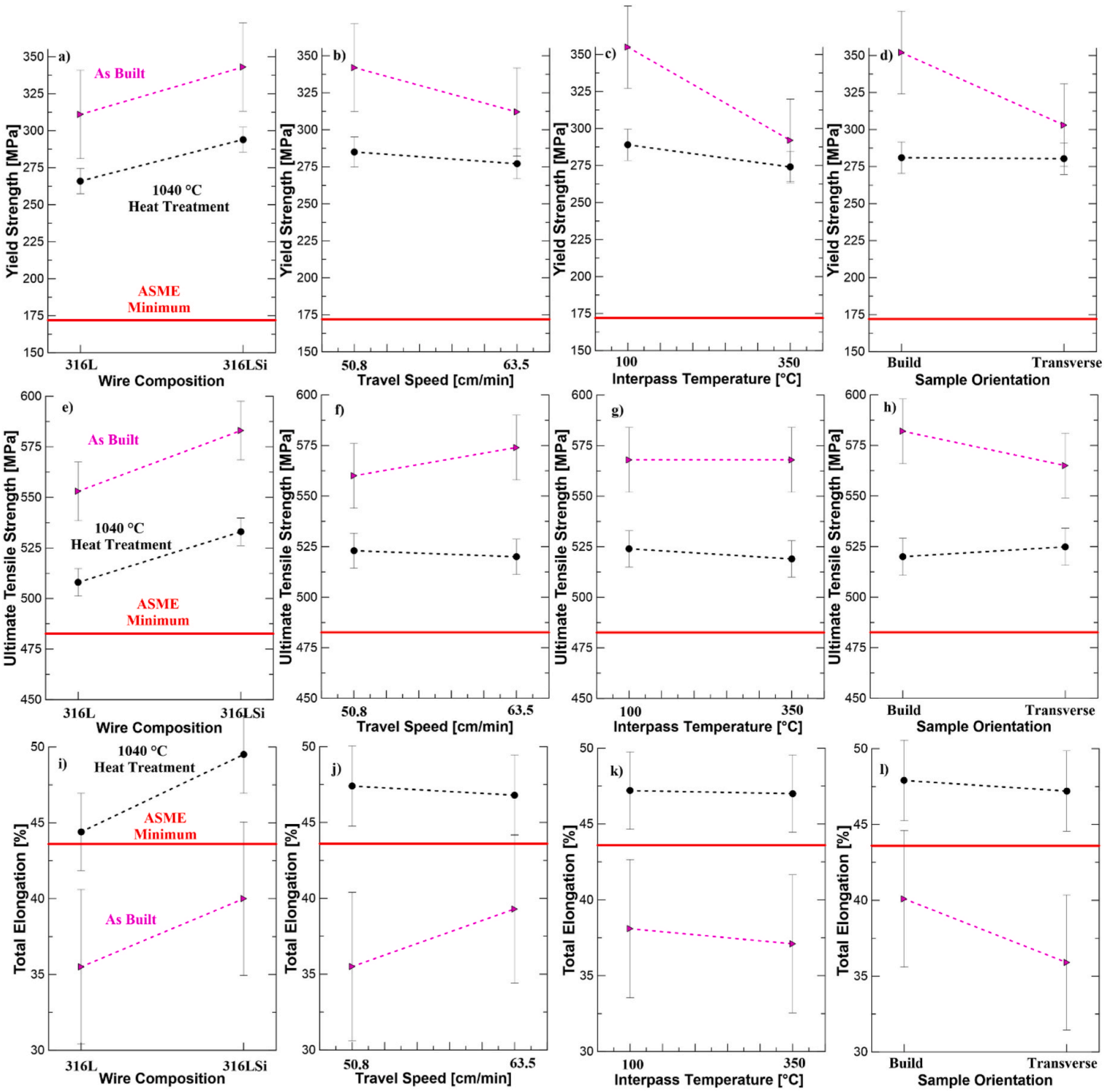

Fig. 4. Effects of wire composition, travel speed, interpass temperature, and tensile test specimen orientation on yield strength (a–d), ultimate tensile strength (e–h) and total elongation (i–l) in comparison with ASME minimums for SA-240 316L at room temperature [38]. The minimum total elongation was converted from 40% elongation in a 50.8 mm (2 in.) gauge length to the equivalent value in a 25.4 mm (1 in.) gauge length using ISO 2566 [39]. In each plot, symbols are mean values and bars are 95% confidence limits based on pooled standard deviations. In the heat treated condition, the means are calculated from 16 measurements, and the for the as-built condition, the means are calculated from 8 measurements.

dimensions and experimental dimensions, shown in Table 10. Additionally, the temperature measurements are affected by spatter on the outside of the walls that cool faster than the wall itself. Other sources of discrepancy may also be latent heat of fusion and convection not being considered within the melt pool, leading to shallower modeled melt pools than the experimental melt pools. It should be noted that the thermal camera was not calibrated for temperatures below 500 °C, so temperatures below 500 °C are not measured by the camera and are not shown in Fig. 9.

For the heat transfer model, the melt pool boundary was defined with a 1440 °C isothermal surface, which is approximately the liquidus temperature of 316L determined from ThermoCalc©. Comparing the observed melt pool with the melt pool shape predicted by the model was also used for model calibration. With the melt pool defined, temperature gradients, *G* were calculated along the melt pool surface. Fig. 10a shows color scaled temperature fields along a plane cut through the melt pool as well vectors that indicate the relative magnitude of the temperature gradient by length. Cooling rate, *C* was also calculated for each point at the solid liquid interface. Solidification velocity, *V*, was then be determined using the relationship $V = C/G$. Fig. 10b shows color scaled cooling rates along the melt pool boundary as well as vectors that indicate relative solidification velocity by length. The bottom of the melt pool (shown on the left side) exhibits larger temperature gradients and lower solidification velocities, whereas the top of the melt pool (on the right side) shows lower temperature gradients and higher solidification velocities.

4.2. *Microstructure predictions of the WA-DED process*

Temperature gradients and solidification velocities for points at the solid liquid interface were then predicted for the full factorial combination of travel speeds and interpass temperatures experimentally evaluated and are shown in Fig. 11. The higher travel velocity (63.5 cm/min) conditions, reach a higher solidification velocity at the tops of the

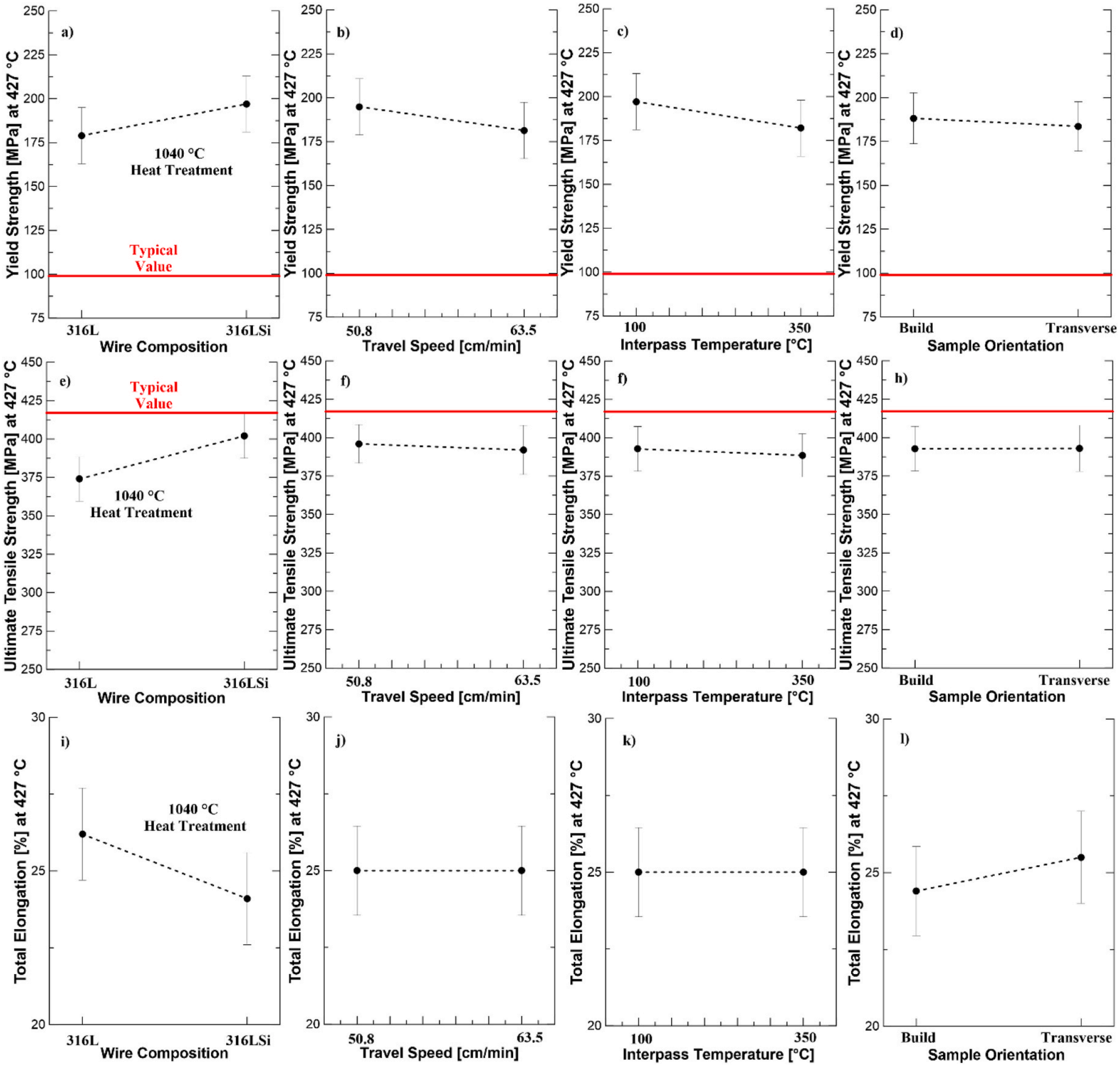

Fig. 5. Effects of wire composition, travel speed, interpass temperature, and tensile test specimen orientation on yield strength (a–d), ultimate tensile strength (e–h) and total elongation (i–l) in comparison with ASME Section II typical values at 427 °C (800 °F) [40]. In each plot, symbols are mean values and bars are 95% confidence limits based on pooled standard deviations. The means are calculated from 16 measurements.

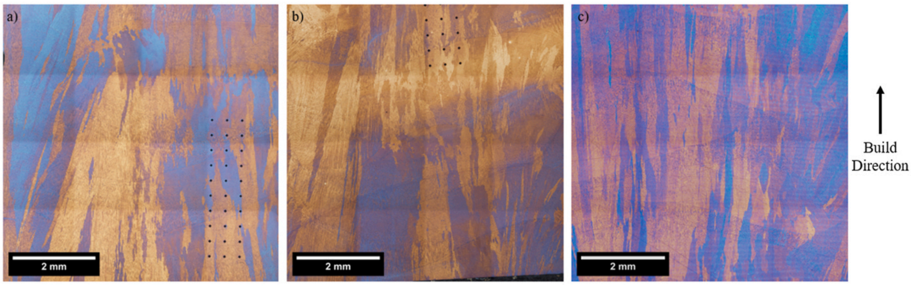

316L – 50.8 cm/min – 100 °C - AB 316LSi – 50.8 cm/min – 100 °C - AB 316LSi – 50.8 cm/min – 100 °C – 1040 °C

Fig. 6. Light optical micrographs after etching with Behera 1 of a) 316L – 50.8 cm/min travel speed – 100 °C interpass temperature – as built (AB) condition b) 316LSi – 50.8 cm/min travel speed – 100 °C interpass temperature – as built condition c) 316LSi – 50.8 cm/min travel speed – 100 °C interpass temperature – 1040 °C condition used for grain width measurements.

melt pools as well as show slightly higher temperature gradients compared to the lower travel velocity conditions. The higher 350 °C interpass temperature conditions display lower temperature gradients than the lower 100 °C interpass temperature conditions. Although interpass temperature appears to have a greater effect on the temperature gradients at the solid liquid interface compared to travel speed, the heat transfer model predicts minor changes across conditions overall, as shown in Fig. 11.

Table 7
Grain width measurements (mean ± 95% confidence limits).

Condition	Average Grain Width (mm)
316L – As Built	0.34 ± 0.07
316LSi – As Built	0.33 ± 0.03
316LSi – 1040 °C Heat Treatment	0.31 ± 0.08

Dendrite arm spacings were then modeled using Equations (6)–(15), using the measured compositions of the builds listed in Table 9, and the prediction results for 316L are shown in Fig. 11. Detailed values from the microstructure prediction models are shown in Supplemental Materials section (Tables 13–18). Experimental dendrite arm spacings were measured from the center of the build towards the bottom of each melt pool, as shown in Fig. 12. The tops of the melt pools are remelted in subsequent passes, so no microstructural measurements were made from these regions. All model predictions shown in Fig. 11 are for 316L, but negligible differences in model predictions or measurements were found between 316L and 316LSi. A plot for 316LSi is shown in Fig. 14 in the Supplemental Materials section. Dendrite growth morphology predictions from the CET model are also shown in Fig. 11. A near completely columnar microstructure is predicted, consistent with what is observed in experimental microstructures shown in Figs. 6 and 7.

Predictions of SDAS and PDAS are compared against experimental measurements in Table 11. Predicted values of G and V for the center of the melt pool, corresponding to where microstructure measurements were taken are also shown. In general, the confidence limits of PDAS and SDAS measurements contain the simulation results, suggesting good agreement. The PDAS and SDAS measurements are predicted to decrease

Table 8
Dendrite arm spacing measurements from parameter DOE (mean ± 95% confidence limits).

Condition	Average PDAS (μm)	Average SDAS (μm)
316L –63.5 cm/min – 100 °C – As-built	25.9 ± 5.1	8.1 ± 1.6
316L –63.5 cm/min – 350 °C – As-built	23.2 ± 5.2	8.9 ± 2.1
316L – 50.8 cm/min – 100 °C – As-built	22.8 ± 5.0	8.6 ± 2.4
316L – 50.8 cm/min – 350 °C – As-built	23.7 ± 4.8	9.1 ± 1.8
316LSi – 63.5 cm/min – 100 °C – As-built	23.0 ± 5.6	8.8 ± 2.1
316LSi – 63.5 cm/min – 350 °C – As-built	23.6 ± 4.1	8.3 ± 1.7
316LSi – 50.8 cm/min – 100 °C – As-built	24.7 ± 4.1	8.4 ± 1.4
316LSi – 50.8 cm/min – 350 °C – As-built	22.3 ± 4.2	8.0 ± 1.9

Table 9
Composition measurements of 316L and 316LSi WA-DED builds (weight %).

Element	316L	316LSi
Iron	Base	Base
Chromium	18.50	18.30
Nickel	12.10	11.01
Molybdenum	2.29	2.18
Silicon	0.35	0.84
Manganese	1.71	1.57
Sulfur	0.015	0.024
Phosphorus	0.021	0.025
Carbon	0.014	0.017
Nitrogen	0.043	0.072
Oxygen	0.055	0.038

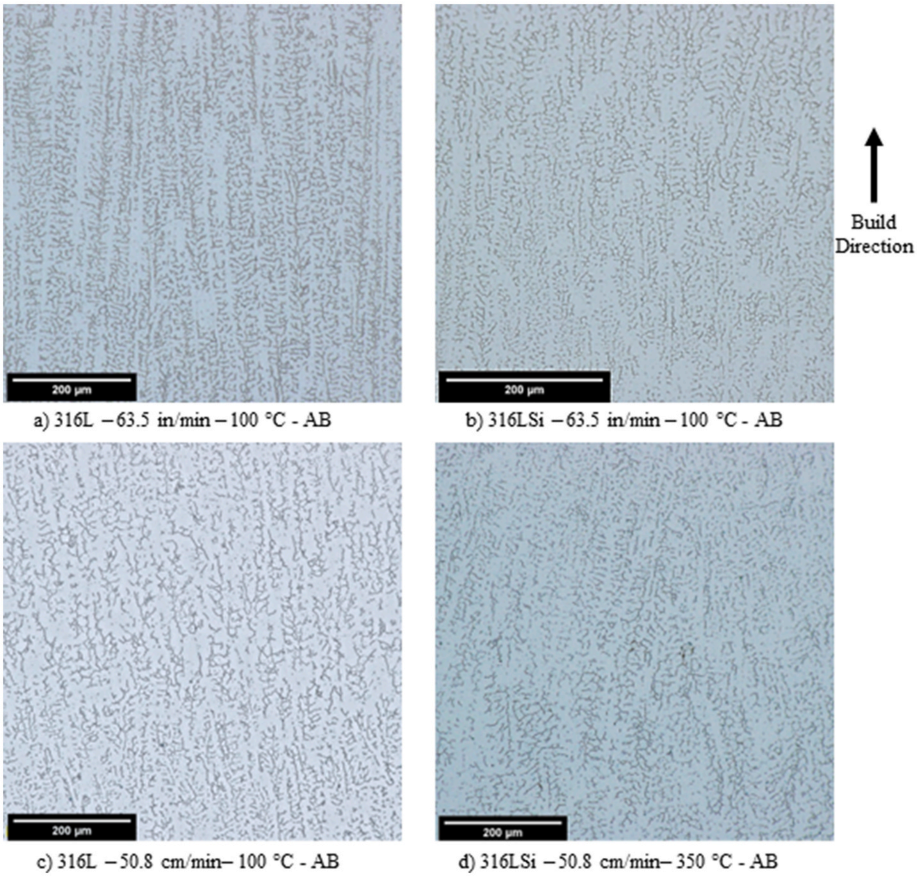

Fig. 7. Light optical micrographs after etching using Glyceregia of a) 316L – 63.5 cm/min travel speed – 100 °C interpass temperature – as built (AB) condition b) 316LSi – 63.5 cm/min travel speed – 100 °C interpass temperature – as built condition c) 316L – 50.8 cm/min travel speed – 100 °C interpass temperature – as built condition d) 316LSi – 50.8 cm/min travel speed – 350 °C interpass temperature – as built condition used for dendrite spacing measurements.

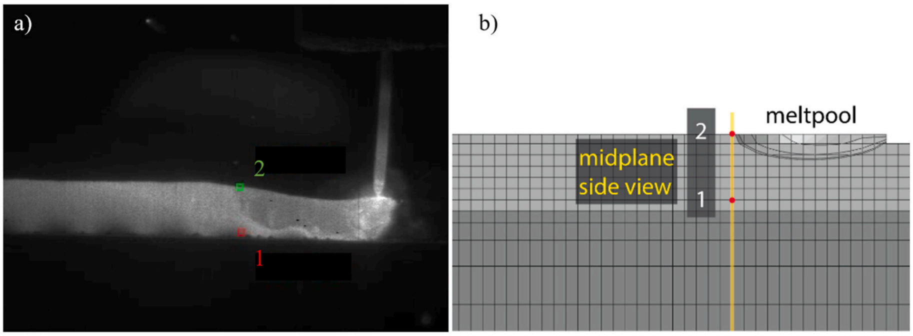

Fig. 8. a) Side view during deposition of 316L, 63.5 cm/min travel speed condition. Point temperature measurements are taken from approximately center length of build and aligned with the top and bottom of the first layer recorded. b) heat transfer model of WA-DED process showing corresponding points.

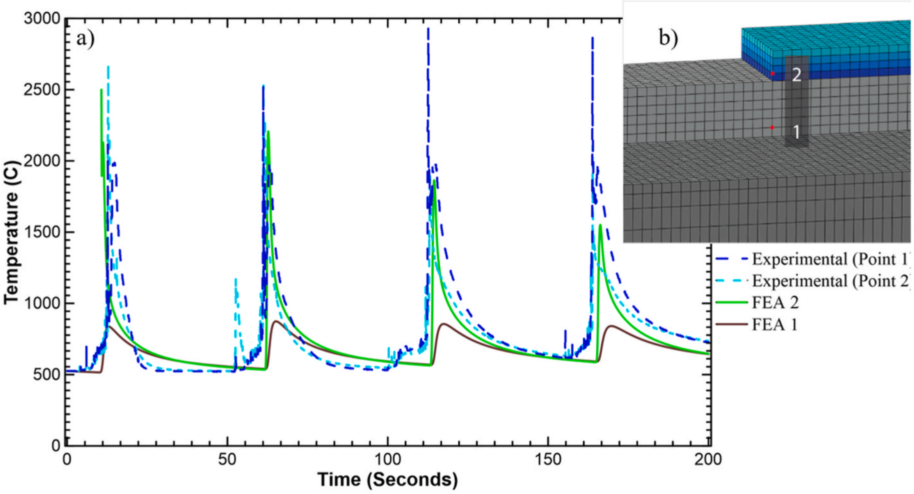

Fig. 9. a) Measured and predicted temperature for 4 deposition passes with the 63.5 cm/min travel speed, 30 s dwell time (350 °C interpass temperature) condition taken from points on the side of the build as shown in b). Experimental (Point 1) and Experimental (Point 2) are temperature measurements taken with the thermal camera corresponding with the top (Point 2) and bottom (Point 1) of the initial melt pool deposited, seen in Fig. 8a. FEA 1 and 2 correspond to heat transfer model temperature predictions for points outlined in b).

Table 10
Melt pool dimensions from experiment and model for the 63.5 cm/min travel speed, 30 s dwell time (350 °C interpass temperature) condition.

Dimension	Experiment	Model
Width (mm)	11.4	7.5
Depth (mm)	5.1	2.2
Length (mm)	21.1	13

with increasing travel speed and decreasing interpass temperature, however there is not a statistically significant difference in measurements between the conditions evaluated. Error in experimental measurements may have arisen from taking dendrite arm spacing measurements from locations not exactly at the center of the melt pools. However, relatively small changes in spacing (less than 4 μm) are predicted within the conditions evaluated. Overall, the combination of heat transfer simulations of WA-DED and solidification models for 316L allowed for microstructure predictions of the as-built condition that are in reasonable agreement with experimental results demonstrating the potential for predicting the influences of processing parameters for process optimization and design.

4.3. Influences of post-build heat treatments on microstructure and mechanical properties

The variation in phase amounts reported for post-build heat treatments at 900, 1040, and 1200 °C each for 1 h followed by water quenching, as shown in Table 6, is generally corroborated by other reports in the literature. Post-build heat treatments at or below 1000 °C that result in the formation of sigma phase generally lead to higher strengths but decreased ductilities, which is unsurprising considering the brittle nature of this intermetallic phase [7,16]. Post build heat treatments above 1000 °C typically result in lower amounts of delta ferrite and sigma phases with correspondingly lower strengths and ductilities. Concomitant with smaller amounts of secondary phases, greater degrees of recovery occur at higher post-build heat treatment temperatures. Wang et al. evaluated dislocation density of WA-DED 316L as a function of post-build heat treatment temperature and showed monotonic decreases in dislocation strengthening with increases in post-build heat treatment temperature from 650 to 1200 °C [16]. Very little change in grain size has been reported from post-build heat treatment in the range of 650–1100 °C because significant recrystallization typically does not occur in this temperature range [7,16]. Partial recrystallization has been reported after heat treating WA-DED 316L at 1200 °C for 1 h [16], although others have shown negligible recrystallization resulting from the same heat treatment [7]. Complete recrystallization has been found after heat treating at 1200 °C for 4 h [7]. Based on evidence in the literature, it can be assumed that decreases in strength and increases in ductility after heat treatment at 1040 and 1200 °C shown in Table 6 are primarily due to reductions in dislocation density from recovery. Furthermore, based on gain size measurements of 316L and 316LSi before and after post-build heat treatment shown in Table 7 and Fig. 6, similarly negligible changes in grain size and thus grain size strengthening are expected between the two alloys.

4.4. Influences of wire composition on mechanical properties

The increase in strength the 316LSi samples over 316L samples is

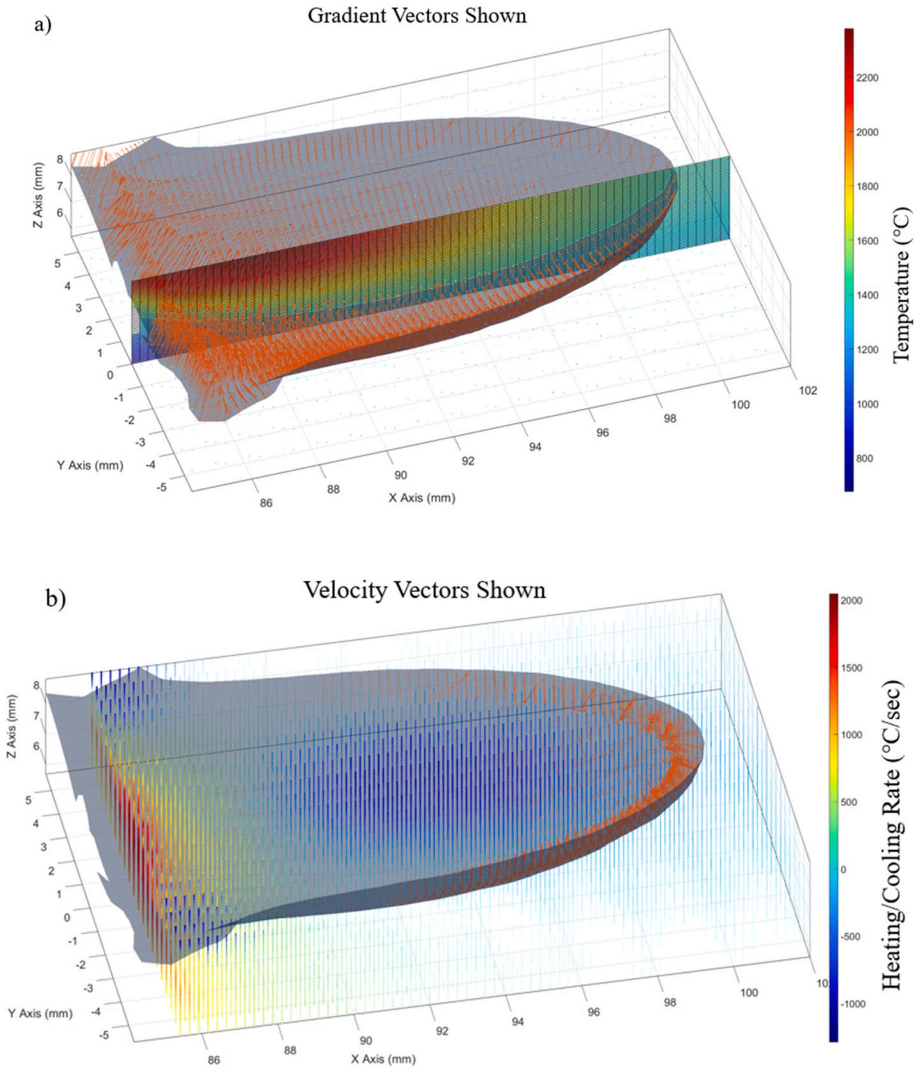

Fig. 10. Heat transfer model results for the 63.5 cm/min travel speed, 30 s dwell time (350 °C interpass temperature) condition. a) 1440 °C isothermal surface showing color coded temperatures along a plane passing through the melt pool. Vectors show relative temperature gradient magnitudes b) 1440 °C isothermal surface showing color coded cooling rates and velocity vectors. In both figures vectors are shown in orange. The melt pool is moving from right to left, so the bottom of the melt pool is on the left and top of the melt pool is on the right of the figures. (For interpretation of the references to color in this figure legend, the reader is referred to the Web version of this article.)

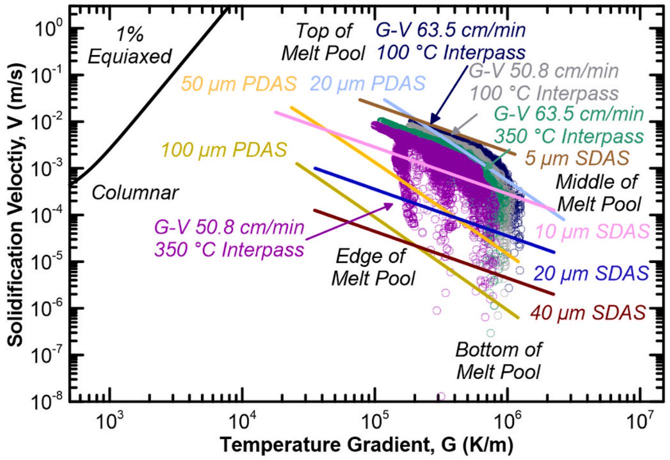

Fig. 11. Temperature gradient (G) and solidification velocity (V) values at the solid liquid interface of WA-DED melt pools from a heat transfer model along with predictions of primary dendrite arm spacing, secondary dendrite arm spacing, and columnar to equiaxed transition models.

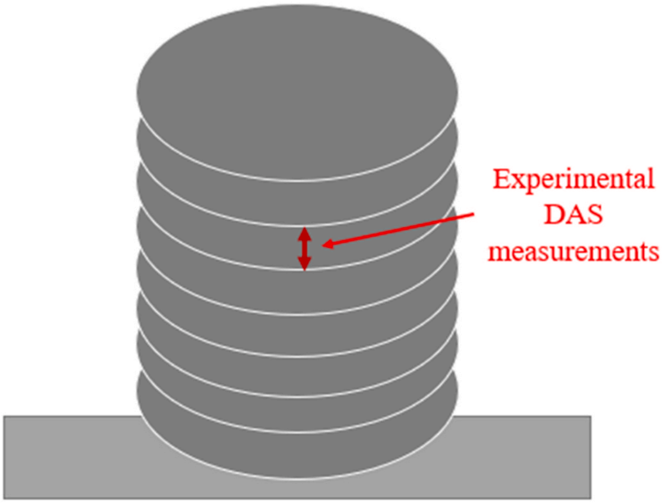

Fig. 12. Diagram showing the regions of melt pools that were not remelting during deposition of subsequent layers, from which dendrite arm spacing measurements could be made.

Table 11
Predicted G, V, PDAS, SDAS and measured PDAS and SDAS from the middle of the melt pool.

Condition (As built)	G (K/m)	V (m/s)	PDAS Predicted (μm)	SDAS Predicted (μm)	PDAS Experimental (μm)	SDAS Experimental (μm)
316L – 50.8 cm/min – 350 °C	$5.8*10^5$	$9.7*10^{-4}$	22.5	7.9	23.7 ± 4.8	9.1 ± 2.1
316L –63.5 cm/min – 350 °C	$6.4*10^5$	$1.2*10^{-3}$	20.3	7.2	23.2 ± 5.2	8.9 ± 2.1
316L – 50.8 cm/min – 100 °C	$6.1*10^5$	$1.9*10^{-3}$	19.1	6.3	22.8 ± 5.0	8.6 ± 2.4
316L –63.5 cm/min – 100 °C	$6.4*10^5$	$1.9*10^{-3}$	18.0	6.2	25.9 ± 5.1	8.1 ± 1.8

likely not a result of microstructure differences, because statistically insignificant changes between grain size and dendrite spacing were observed across samples. It is possible that the differences in wire composition between 316L and 316LSi lead to differences in solid solution strengthening. Eliasson and Sandström have previously shown that at room temperature, silicon strengthens austenitic stainless steels with a factor of 23 MPa/wt.% Si [41]. From the composition analysis, the 316LSi samples contain approximately 0.49 wt% more silicon than the 316L samples leading to an expected increase in yield strength of 11.3 MPa. The 316LSi filler wire used in this study also contained 0.03 wt % more nitrogen than the 316L filler wire. Eliasson and Sandström have shown that N is a potent solid solution strengthener, with an expected strengthening factor of over 800 MPa/wt.% N [41]. The resulting expected increase in yield strength from nitrogen solid solution strengthening would be approximately 24 MPa. At room temperature, in the heat-treated condition, an increase in yield strength of 28 ± 10 MPa was observed in 316LSi compared to 316L. The measured difference in yield strength is slightly lower than the expected increase in yield strength from solid solution strengthening of both silicon and nitrogen (35.3 MPa), but the expected increase does fall within the experimental confidence interval. It is possible that unaccounted for differences in other element concentrations between 316LSi and 316L lead to lower-than-expected differences in strength.

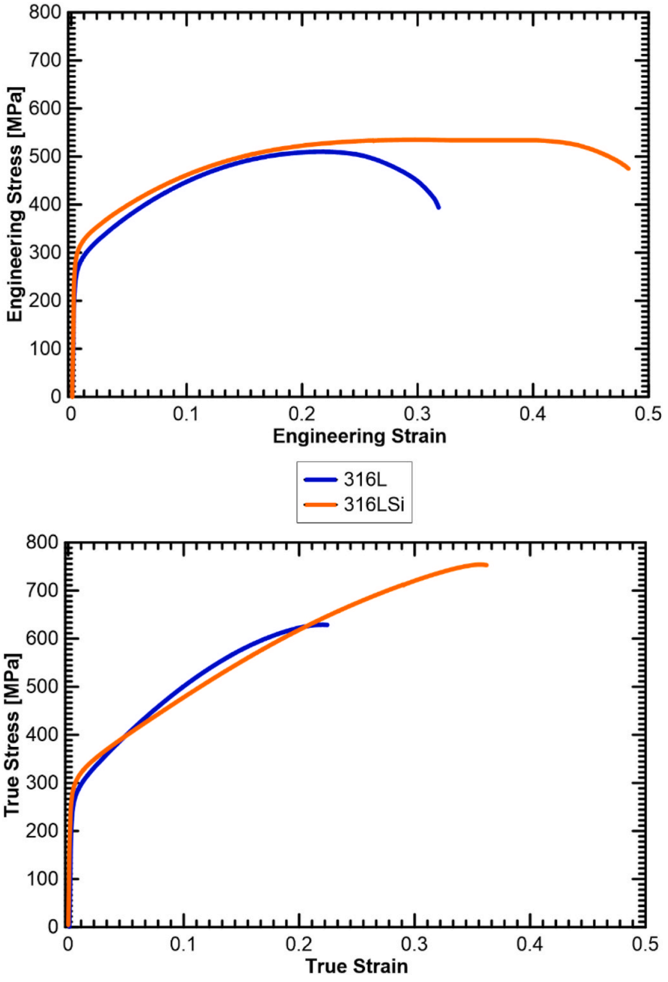

Fig. 13. Engineering and True stress and strain for 316L and 316LSi specimens from the transverse direction built with a 50.8 cm/min travel speed and a 350 °C interpass temperature.

Eliasson and Sandström also show the solid solution strengthening effect of silicon and nitrogen decrease with increasing temperature. At 427 °C they predict a strengthening factor of approximately 7 MPa/wt.% Si and 400 MPa/wt.% N [41]. Based on solid solution strengthening contributions from differences in silicon and nitrogen contents, 316LSi would be expected to have 15 MPa higher yield strength than 316L at 427 °C. After testing at 427 °C, the 316LSi samples in this work display a 18 ± 30 MPa increase in yield strength compared than 316L samples, although the measured increase is not statistically significant.

The increase in ductility observed in 316LSi samples is likely not a result of solid solution strengthening. Fig. 13 shows engineering and true stress strain curves of one 316L and one 316LSi sample both built with a 50.8 cm/min travel speed, a 350 °C interpass temperature, and tested in the transverse direction. The engineering stress strain curves show that the major difference in ductility between the 316L and 316LSi samples is uniform elongation. Table 12 shows values of uniform and post-unform elongation for 316L and 316LSi indicating that the greater ductility in 316LSi is primarily due to a higher uniform elongation. From the true stress strain curve shown in Fig. 13, it can be seen that after yielding, the 316L sample initially displays a higher strain hardening rate compared to the 316LSi sample. However, the 316LSi sample maintains a higher strain hardening rate to higher strains leading to the greater uniform elongation with 316LSi. Previous literature has shown that silicon lowers and nickel raises stacking fault energy in austenitic stainless steels [42,43]. It is likely that the higher silicon and lower nickel content in 316LSi results in a lower stacking fault energy compared to 316L. Hence, cross slip is suppressed in 316LSi during tensile deformation thus delaying dynamic recovery and necking to larger strains, which results in a higher uniform elongation. The increases in mechanical performance of 316LSi based on composition reported here show the potential for the development of new austenitic stainless steel alloys with improved strength and ductility for WA-DED applications.

Table 12
Uniform and post-uniform elongation for 316L and 316LSi wire compositions.

	% Elongation	% Uniform Elongation	% Post Uniform Elongation
316LSi Average	49.5	34.5	15.0
316L Average	44.4	30.2	14.2

4.5. *Elevated temperature mechanical performance of WA-DED*

At 427 °C (800 °F), samples from the parametric study exceeded typical values for YS but were slightly below typical values for UTS. The low values of UTS in WA-DED samples may be attributed to the large grain size relative to the specimen size. Previous work has shown that a large grain size in comparison to the tensile specimen geometry can lower strain hardening rates, possibly leading to lower UTS values at 427 °C [44]. Further work is needed to validate WA-DED 316L for high temperature applications, and elevated temperature tensile testing with larger tensile specimens can be used to evaluate any changes in strain hardening. It is interesting to note that due to the large grain size observed, WA-DED 316L is expected to have good creep performance, as the large grains minimize the potential for grain boundary sliding [45]. Creep testing presents another opportunity for future study of WA-DED 316L for high temperature structural applications.

4.6. *Influence of travel speed, interpass temperature, and sample orientation*

From the parametric study, interpass temperature and travel speed showed minimal influence on the mechanical properties and microstructure in the heat-treated condition. Changing these processing parameters resulted in no significant change in grain size, dendrite spacing, yield strength, tensile strength, or ductility. High deposition rate WA-DED, as studied here, has a limited processing window within which shape accuracy during the building process can be maintained. Changes to travel speed and interpass temperature within this operating range were likely not large enough to significantly impact microstructure and thus mechanical properties. Additionally, sample orientation showed minimal effect on mechanical properties, despite the strongly oriented columnar grains observed. This may be due to the large grain size and correspondingly small boundary strengthening component in the microstructure.

4.7. *Comparison of room temperature mechanical properties of WA-DED to other additive manufacturing processes*

The mechanical properties of WA-DED 316L and 316LSi reported here generally show lower strengths and higher ductilities compared to other forms of 316L processed with laser powder directed energy deposition (LP-DED) and laser powder bed fusion (LPBF). As an example, yield strengths in the as-built condition range from 405 to 485 MPa for LP-DED [46] and 425–500 MPa for LPBF [47]. Total elongations on subsized specimens reported by the same authors vary between 12 and 40% for LP-DED [46] and 2–25% for LPBF in the as-built condition. Generally, strengths decrease and total elongations increase with post build heat treatment for LP-DED and LPBF in the studies referenced, but the total elongations reported here and elsewhere for WA-DED 316L are generally higher and meet or exceed ASTM minimum values at room temperature. The generally higher ductilities in WA-DED, combined with larger grain sizes and the potential for superior creep resistance may favor WA-DED for the production of large scale components for high temperature power generation where ASTM mechanical property targets are a design criteria.

5. Conclusions

The microstructure and mechanical properties of high deposition rate WA-DED of 316L and 316LSi were investigated using a combination of experiments and models. From the results presented here, the following conclusions are made.

- Post-build heat treatment is an effective way of tuning the phase distribution present in the as-built condition, but it has little effect on grain morphology and grain size. The as-built condition showed large, columnar austenite grains with skeletal ferrite and a small amount of sigma phase. Post-build heat treatments at temperatures ranging from 900 °C to 1200 °C altered the phase fractions present. A heat treatment of 1040 °C for 1 h and water quenching resulted in a near elimination of the brittle sigma phase, thus increasing ductility from the as-built condition while maintaining strength.
- After heat treatment at 1040 °C, specimens from a parametric study examining the influence of travel speed, interpass temperature, and wire composition successfully met ASME strength and ductility room temperature minimums for 316L; however, specimens from the as-built condition failed to meet minimum room temperature ductility requirements.
- Travel speed and interpass temperature had minimal impact on microstructure or mechanical properties, but the 316LSi wire composition displayed significantly increased ductility, yield strength, and tensile strength over 316L. Because the grain size and dendrite spacings were not significantly different between 316L and 316LSi, the increase in strength is likely a result of solid solution strengthening from higher silicon and nitrogen contents in 316LSi. The increased ductility in 316LSi samples observed in this work is attributed to the lower stacking fault energy due to higher silicon and lower nickel contents compared to 316L. The improved mechanical performance of 316LSi, based primarily on composition, shows the potential for designing new austenitic stainless steel wire feedstocks for improved performance manufactured with WA-DED.
- At 427 °C (800 °F), specimens exceeded ASME typical values for yield strength, but tensile strengths were slightly below typical values. The lower-than-expected tensile strengths measured in this work is possibly due to the large grain size relative to the tensile specimens utilized.
- A heat transfer model was successfully developed to predict the thermal history of WA-DED builds. Predictions from the heat transfer model in combination and dendrite arm spacing and morphology models agreed with experimental measurements demonstrating the possibility of modeling the effects of WA-DED process parameters to aid in process design and optimization.

Funding

This research is supported by the National Science Foundation with Award No. 1822144.

CRediT authorship contribution statement

Luc Hagen: Formal analysis, Investigation, Methodology, Writing – original draft, Writing – review & editing. **Zhenzhen Yu:** Writing – review & editing. **Amy Clarke:** Writing – review & editing. **Kester Clarke:** Writing – review & editing. **Stephen Tate:** Conceptualization, Writing – review & editing. **Anthony Petrella:** Methodology, Supervision, Writing – review & editing. **Jonah Klemm-Toole:** Conceptualization, Supervision, Methodology, Writing – review & editing.

Declaration of competing interest

The authors declare that they have no known competing financial interests or personal relationships that could have appeared to influence the work reported in this paper.

Data availability

Data will be made available on request.

Acknowledgements

The authors gratefully acknowledge the support of sponsors from the Manufacturing and Materials Joining Innovation Center (Ma2JIC), and

National Science Foundation (NSF) Industry University Collaborative Research Center (IUCRC).

Appendix A. Supplementary data

Supplementary data to this article can be found online at https://doi.org/10.1016/j.msea.2023.145044.

References

[1] Annamaria Gisario, et al., Metal additive manufacturing in the commercial aviation industry: a review, J. Manuf. Syst. 53 (2019) 124–149.

[2] Desu, Raghuram Karthik, et al., Mechanical properties of austenitic stainless steel 304L and 316L at elevated temperatures, J. Mater. Res. Technol. 5 (1) (2016) 13–20.

[3] J.C. Lippold, V.F. Savage, Solidification of austenitic stainless steel weldments: Part I—a proposed mechanism, Weld J. 58 (1979) 362–374.

[4] William E. Frazier, Metal additive manufacturing: a review, J. Mater. Eng. Perform. 23 (6) (2014) 1917–1928.

[5] Hiroshige Inoue, Toshihiko Koseki, Solidification mechanism of austenitic stainless steels solidified with primary ferrite, Acta Mater. 124 (2017) 430–436.

[6] W.T. DeLong, Ferrite in Austenitic Stainless Steel Weld Metal, 1974.

[7] Xiaohui Chen, et al., Effect of heat treatment on microstructure, mechanical and corrosion properties of austenitic stainless steel 316L using arc additive manufacturing, Mater. Sci. Eng., A 715 (2018) 307–314.

[8] C.R. Cunningham, et al., Characterisation of austenitic 316 LSi stainless steel produced by wire arc additive manufacturing with interlayer cooling, in: 2019 International Solid Freeform Fabrication Symposium, University of Texas at Austin, 2019.

[9] Amanda S. Wu, et al., An experimental investigation into additive manufacturing-induced residual stresses in 316L stainless steel, Metall. Mater. Trans. 45 (13) (2014) 6260–6270.

[10] Rosli, Nor Ana, et al., Review on effect of heat input for wire arc additive manufacturing process, J. Mater. Res. Technol. 11 (2021) 2127–2145.

[11] J.W. Elmer, S.M. Allen, T.W. Eagar, Microstructural development during solidification of stainless steel alloys, Metall. Trans. A 20 (10) (1989) 2117–2131.

[12] Amagoia Paskual, Álvarez Pedro, Alfredo Suárez, Study on arc welding processes for high deposition rate additive manufacturing, Procedia Cirp 68 (2018) 358–362.

[13] Stewart W. Williams, et al., Wire + arc additive manufacturing, Mater. Sci. Technol. 32 (7) (2016) 641–647.

[14] Lincoln Electric, Blue Max Mig 316L, Blue Max® MiG 316L. https://www.lincolnelectric.com/en/products/bluemaxmig316l_gmaw.

[15] Linclon Electric, Lincoln® Red Max® 316LSi, LINCOLN® red Max® 316LSi. https://www.lincolnelectric.com/en/Products/lincolnredmax316lsi_gmaw?sku=ED036768.

[16] C. Wang, et al., Effect of heat treatment temperature on microstructure and tensile properties of austenitic stainless 316L using wire and arc additive manufacturing, Mater. Sci. Eng., A 832 (2022), 142466.

[17] Rodriques, A. Tiago, et al., Effect of heat treatment on 316 stainless steel parts fabricated by wire and arc additive manufacturing: microstructure and synchrotron X-ray diffraction analysis, Addit. Manuf. 48 (2021), 102428.

[18] ASTM SA-480/SA-480M - 22, Specification for General Requirements for Flat-Rolled Stainless and Heat Resisting Steel Plate, Sheet, and Strip, ASTM International, 2022.

[19] ASTM E8/E8M-22, Standard Test Methods for Tension Testing of Metallic Materials, ASTM International, 2022.

[20] Vander Voort, F. George, et al., ASM handbook, Metal. Microstruct. 9 (2004), 44073-0002.

[21] Katharine B. Small, David A. Englehart, Todd A. Christman, Etching specialty alloys, Adv. Mater. Process. (2008) 33.

[22] Peter Pichler, et al., Measurements of thermophysical properties of solid and liquid NIST SRM 316L stainless steel, J. Mater. Sci. 55 (9) (2020) 4081–4093.

[23] British Stainless Steel Association, Elevated temperature physical properties of stainless steels. https://bssa.org.uk/bssa_articles/elevated-temperature-physical-properties-of-stainless-steels/. (Accessed 10 October 2020).

[24] Hiroyuki Fukuyama, Hideo Higashi, Hidemasa Yamano, Thermophysical properties of molten stainless steel Containing 5 mass % B4C, Nucl. Technol. 205 (9) (2019) 1154–1163.

[25] John A. Goldak, Akhlaghi Mehdi, Computational Welding Mechanics, Springer Science & Business Media, 2005.

[26] Frédéric Valiorgue, et al., Emissivity calibration for temperatures measurement using thermography in the context of machining, Appl. Therm. Eng. 58 (1–2) (2013) 321–326.

[27] W.1. Kurz, B. Giovanola, R. Trivedi, Theory of microstructural development during rapid solidification, Acta Metall. 34 (5) (1986) 823–830.

[28] T. Umeda, T. Okane, W. Kurz, Phase selection during solidification of peritectic alloys, Acta Mater. 44 (10) (1996) 4209–4216.

[29] F. Mas, C. Tassin, F. Roch, M. Yesca, P. Todeschini, Y. Brechet, Growth morphologies and primary solidification modes in dissimilar weld between a low-alloy steel and an austenitic stainless steel, Metals 8 (4) (2018) 284.

[30] Jonathan A. Dantzig, Michel Rappaz, Solidification: -Revised & Expanded, EPFL press, 2016.

[31] J. Lipton, M.E. Glicksman, W. Kurz, Dendritic growth into undercooled alloy metals, Mater. Sci. Eng. 65 (1) (1984) 57–63.

[32] J. Lipton, M.E. Glicksman, W. Kurz, Equiaxed dendrite growth in alloys at small supercooling, Metall. Mater. Trans. 18 (2) (1987) 341–345.

[33] Mark Easton, Cameron Davidson, John David St, Effect of alloy composition on the dendrite arm spacing of multicomponent aluminum alloys, Metall. Mater. Trans. 41 (6) (2010) 1528–1538.

[34] M. Gäumann, et al., Single-crystal laser deposition of superalloys: processing–microstructure maps, Acta Mater. 49 (6) (2001) 1051–1062.

[35] M. Gäumann, R. Trivedi, W. Kurz, Nucleation ahead of the advancing interface in directional solidification, Mater. Sci. Eng., A 226 (1997) 763–769.

[36] C.R. Cunningham, et al., Effects of in-process LN2 cooling on the microstructure and mechanical properties of type 316L stainless steel produced by wire arc directed energy deposition, Mater. Lett. 282 (2021), 128707.

[37] Qi Chao, et al., The effect of post-processing heat treatment on the microstructure, residual stress and mechanical properties of selective laser melted 316L stainless steel, Mater. Sci. Eng., A 821 (2021), 141611.

[38] ASME 1998 Section II, ASME SA-240/SA-240M, "Specification for Heat-Resisting Chromium and Chromium-Nickel Stainless Steel Plate, Sheet, and Strip for Pressure Vessels, ASME Press, New York, NY, 1998.

[39] ISO 2566-1:2021, Steel — Conversion of Elongation Values — Part 1: Carbon and Low-Alloy Steels, ISO, 2021.

[40] ASME Section II Part D Tables U and Y-1, ASME Press, 2019, pp. 722–725, 586-587.

[41] Johan Eliasson, Rolf Sandström, Proof strength values for austenitic stainless steels at elevated temperatures, Steel Res. 71 (6–7) (2000) 249–254.

[42] Toshio Yonezawa, et al., The effect of chemical composition and heat treatment conditions on stacking fault energy for Fe-Cr-Ni austenitic stainless steel, Metall. Mater. Trans. 44 (13) (2013) 5884–5896.

[43] Kookhyun Jeong, et al., The effects of Si on the mechanical twinning and strain hardening of Fe–18Mn–0.6 C twinning-induced plasticity steel, Acta Mater. 61 (9) (2013) 3399–3410.

[44] Whitney Poling, Grain Size Effects in Micro-tensile Testing of Austenitic Stainless Steel, Colorado School of Mines, 2012.

[45] Oleg D. Sherby, Eric M. Taleff, Influence of grain size, solute atoms and second-phase particles on creep behavior of polycrystalline solids, Mater. Sci. Eng., A 322 (1–2) (2002) 89–99.

[46] Aref Yadollahi, et al., Effects of the process time interval and heat treatment on the mechanical and microstructural properties of direct laser deposited 316L stainless steel, Mater. Sci. Eng., A 644 (2015) 171–183.

[47] Tobias Ronneberg, Catrin M. Davies, Paul A. Hooper, Revealing relationships between porosity, microstructure and mechanical properties of laser powder bed fusion 316L stainless steel through heat treatement, Mater. Des. 189 (2020), 108481.